STORT Hypersonic Flight Experiment Forebody Temperature Results

T. Reimer¹, G. D. Di Martino¹, L. Dauth², L. Baier¹, A. Gülhan³, F. Klingenberg³, D. Hargarten⁴

¹DLR Institute of Structures and Design, 70569 Stuttgart, Germany

²Bayern-Chemie GmbH, 84544 Aschau am Inn, Germany

³DLR Institute of Aerodynamics and Flow Technology, 51147 Cologne, Germany

⁴DLR Space Operations and Astronaut Training, 82234 Wessling, Germany

Abstract

The objective of the DLR project STORT was to investigate key technologies for flight at hypersonic Mach numbers of approximately 8. The reason is, that a cost reduction of future space transportation systems is required while keeping them reliable. Therefore, also the stages of a launcher system need to be fully reusable. For first stages, a Mach number of around 8 seems to be a suitable staging velocity, for which technologies for the return flight need to be developed and validated. Consequently, STORT aimed at achieving such operating conditions to support the optimization and validation of technologies and simulation tools for the development of future space transportation systems.

The present paper briefly describes the design, manufacturing and integration of the forebody assembly which required a ceramic matrix composite thermal protection system made from C/C-SiC structures built in-house by DLR.

Mainly, the flight results in terms of measured temperatures on the forebody structures are presented in detail and some of the data is processed to achieve more information about the thermal environment, in particular the heat flux as the driving force for the temperatures.

Keywords: Ceramic Matrix Composites, Thermal Protection System, Hypersonic Flight Experiment

1. Introduction

The development and optimization of space transportation systems is done to a great extent via the use of numerical tools. In order to validate those tools and make them reliable, they need to be tested and calibrated against real measured data. Such data may come from ground experiments in wind tunnels but these facilities often have restrictions and cannot replicate the real flight environment, so flight experiments are very important to collect relevant data. Sounding rocket flight experiments provide for a cost-efficient opportunity to collect such flight data in a real flight environment if the targeted flight regime can be achieved. With this goal in mind, DLR has been working on a number of experimental flight test projects over recent years with the objective of demonstrating technologies for reusable first stage launchers. While such previous and ongoing DLR projects focus on aerodynamics and control at Mach numbers lower than 5 [1, 2, 3] with correspondingly moderate heat loads, the focus of the STORT project [4] was on the thermomechanical challenges encountered by thermally highly loaded components at high Mach numbers (at or higher than 8) for a relatively long time, of approximately 2 minutes. To illustrate the targeted flight conditions, in Figure 1 the nominal trajectory is shown.

As a result, high heat loads were encountered for a relatively long time, thus obtaining more representative conditions of high-energetic re-entry flights for application in reusable first or even upper stages. In this framework, the DLR Institute of Structures and Design was responsible for the design, manufacture, assembly and testing of the forebody of the sounding rocket for the flight experiment. The external structures were subjected to high heat loads and mechanical loads during the flight, therefore they needed to be made of ceramic matrix composite (CMC) materials and the design process had to consider a challenging thermo-mechanical environment.

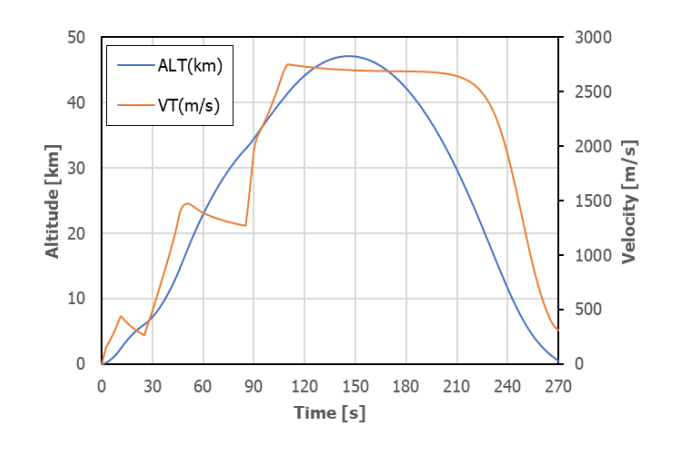


Figure 1: STORT flight experiment nominal trajectory.

2. Structure concept and material

The main requirement for the design was to obtain a smooth external surface, which would allow to investigate the aerodynamic phenomena typical of the hypersonic flow. In order to reduce the number of parts, the forebody aerodynamic surface consisted of a bulk nose and four axisymmetric CMC shell segments, which provided for the thermal protection system (TPS) of the launcher forebody. They consisted of an in-house manufactured CMC structure, also called C/C-SiC which is a carbon fiber-reinforced ceramic, where the matrix is a mix of amorphous carbon, silicon carbide and small amounts of residual silicon. The processing sequence is as follows:

- Manufacturing of the green body CFRP part via wet filament winding
- Pyrolysis to create an intermediate stage C/C component
- In-situ joining of the connection elements in C/C condition
- Reactive melt infiltration with liquid silicon to create the C/C-SiC final component

In order to provide attachment points to the wound CMC shell structures, the in-situ joining method [5], was implemented to attach CMC brackets to the insides of the shell structures. Thus, the TPS could be connected to the metallic understructure while avoiding surface disturbances which would affect the external aerodynamic flow. Figure 2 shows a view of the CMC shell segment B from the outside in the final condition and an internal view where the CMC brackets for attachment and some sensor fixation points are joined to the shell.



Figure 2: STORT shell segment B in the final machined C/C-SiC condition (left); internal view on the in-situ joined CMC brackets and instrumentation reception points (right).

In Figure 3 the typical assembly process is shown for the example of segment D. First, the metallic connection elements are mounted to the ceramic brackets of the shell and the sensors are attached to the shell at their positions. Next, the internal insulation is placed inside of the shell and finally the metallic structure is inserted and the connection elements are connected to the metallic structure. These pre-assembled segments are then stacked on top of each other and connected to arrive at the completed forebody, shown in Figure 4.



Figure 3: Assembly sequence with sensor integration, insulation placement and metallic structure plus equipment integration, shown for the example of segment D.



Figure 4: CMC forebody of STORT.

3. Thermo-mechanical structure validation

Numerical simulations were done to analyze the forebody structures in order to support the design process and validate the overall resistance of the structures.

First, an estimation of the thermal response of the CMC thermal protection system surface structures was obtained by an iterative procedure based on the general equation for the convective heat flux where the heat transfer coefficient was estimated with literature correlation equations [6] for the different segments, and the recovery temperature was estimated based on the trajectory data. The estimated heat flux was given as boundary condition, together with the radiation energy emission of the body to the external environment, for a transient thermal simulation. Figure 5 shows the results in terms of maximum wall temperature and convective heat flux expected during the trajectory on the tip of the structure. Such calculations were also carried out for the structures further downstream. More details on the preliminary thermal simulation model and results can be found in [7]. It has to be said that the procedure did not take into account transition effects of the flow.

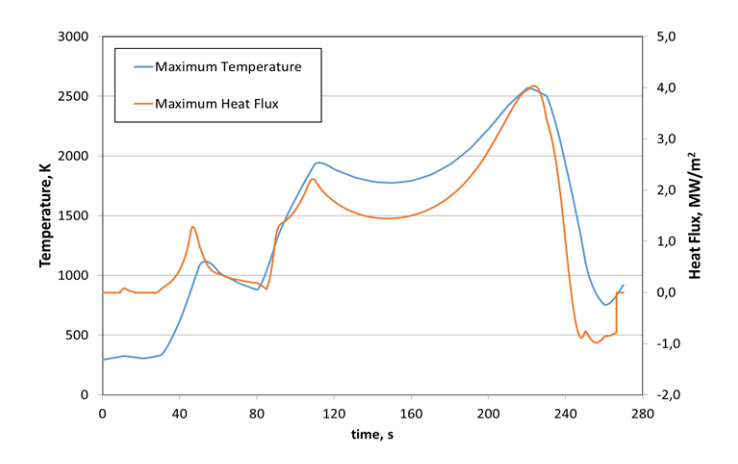


Figure 5: Calculated maximum wall temperature and convective heat flux on the structure tip.

The calculated temperature distributions were then considered as load conditions for a static mechanical analysis to estimate the structure thermal expansion and the associated stresses. Other load cases for the structure validation included the expected most critical aerodynamic pressure load, axial and transversal acceleration loads and vibration load. The results of the structural simulations can be found in [7].

4. Sensor Positions

The flight of the STORT experimental vehicle was fully successful. The data of the sensors installed in the TPS could be transmitted via telemetry to the ground station until the vehicle was at a low altitude. In Figure 6 the axial thermocouple positions in the forebody are presented along the $\varphi=45^\circ$ line with their denominations. Similar sensor positions in terms of axial position existed on the 135°, 225° and 315° line. The angle φ describes the angular position around the vehicle longitudinal axis pointing from the tip to the aft of the vehicle. On the planes at $\varphi=0^\circ$, 90°, 180° and 270°, there were pressure and heat flux sensors as well as so-called combined sensors with pressure, heat flux and temperature in one sensor head, but these measurements will not be detailed here.

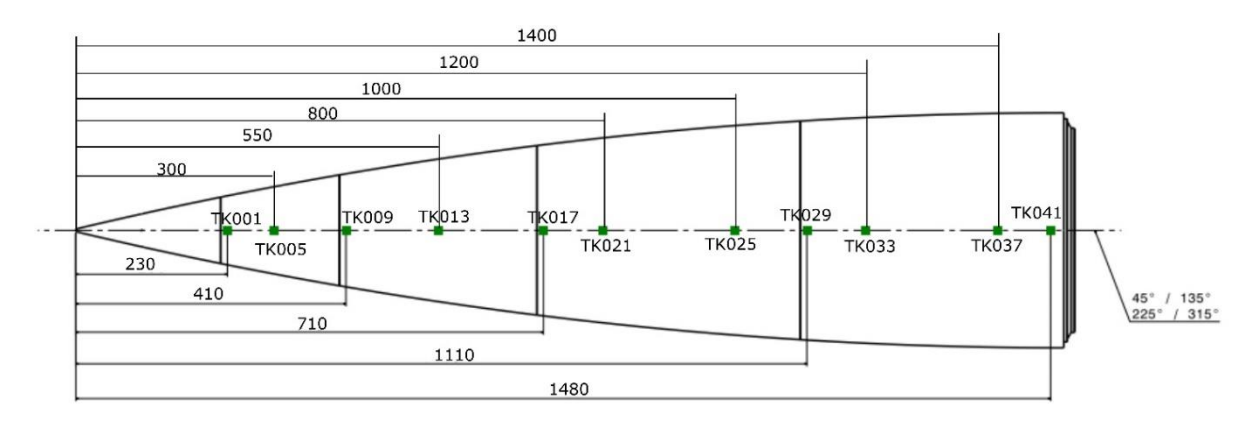


Figure 6: Axial thermocouple positions on the STORT CMC forebody with name tag for the 45°-line. TCs were positioned on four lines from the stagnation point downstream separated by 90° angles.

The thermocouples TK001 up to TK041 shown in Figure 6 were of type K; they were placed in the CMC structures that formed the outer shell of the TPS. As a rule, they were placed in grooves in the CMC material which were machined in such a way so that the measurement was at a depth of 2 mm below the surface. The thermocouple tip was placed in the center of the groove and the groove was then filled with a graphite adhesive to keep it secured and in place. The groove was produced in the circumferential direction so that the thermocouple would follow the isothermal in the structure for

the length of the groove to avoid an influence on the measured value due to thermal gradients along the axial direction of the forebody. The actual situation is shown as an example in Figure 7.

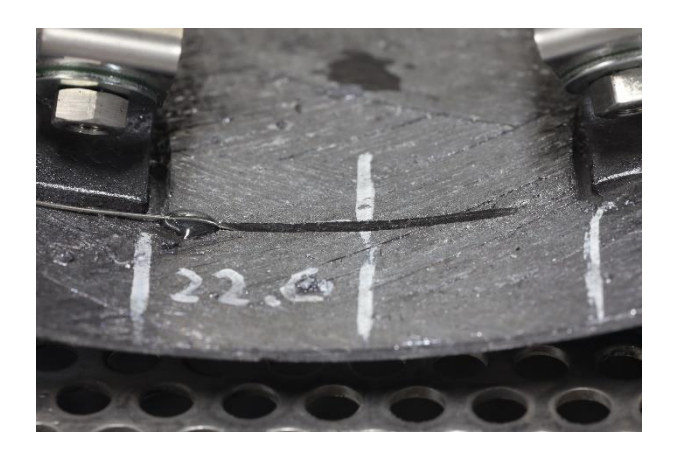


Figure 7: Machined groove and thermocouple entering the groove.

In Figure 8 the thermocouple positions in the nose tip are depicted and Table 1 gives the corresponding numbers. The nose was machined from a solid block of C/C-SiC material. Narrow holes were produced via electrical discharge machining starting from the end of the nose to place the thermocouples inside. Four holes were created and thermocouples of type S were installed. TS001 and TS002 were on the axial position of 34 mm behind the stagnation point, with TS001 on the nose axis and TS002 at a radius of 5 mm from the axis and at a distance of 5 mm below the surface in radial direction. TS003 and TS004 were further behind at 150 mm from the stagnation point and a radial distance from the surface of 9 mm and 3 mm respectively. Unortunately, late during the assembly process of the forebody, the TS001 thermocouple was destroyed accidentally and so the TS002 thermocouple was the most forward sensor position in the vehicle.

Table 1: Thermocouple positions in the tip.

Name	Туре	Axial position from stagnation	Radial distance from surface
		mm	mm
TS001	S	34	10
TS002	S	34	5
TS003	K	150	9
TS004	K	150	3

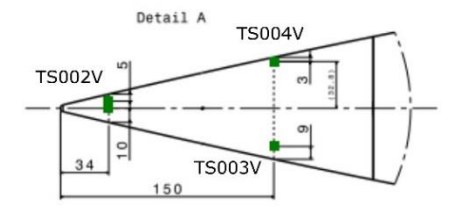


Figure 8: Thermocouple positions in the STORT nose tip.

5. Flight Results

In order to give a general overview of the achieved flight conditions, the Mach number and the altitude are presented first, each with the flight data and the prediction in comparison. Then, the times of the characteristic events during the flight are given in Table 2. In Figure 9a the altitude graphs are depicted, the achieved maximum altitude during flight was 38 km, compared to 46 km as predicted. The difference between flight data and prediction is mainly due to a slightly delayed ignition of the third stage, resulting in a lower elevation angle at ignition of the third stage. Though the altitude was lower than expected, the heat loads were higher due to the higher atmospheric density. In Figure 9b the Mach number graphs are shown. As a result of the lower altitude and the higher density, the Mach number was lower than expected but still above Mach 8 for the initial part of the flight and very close to it for about one minute.

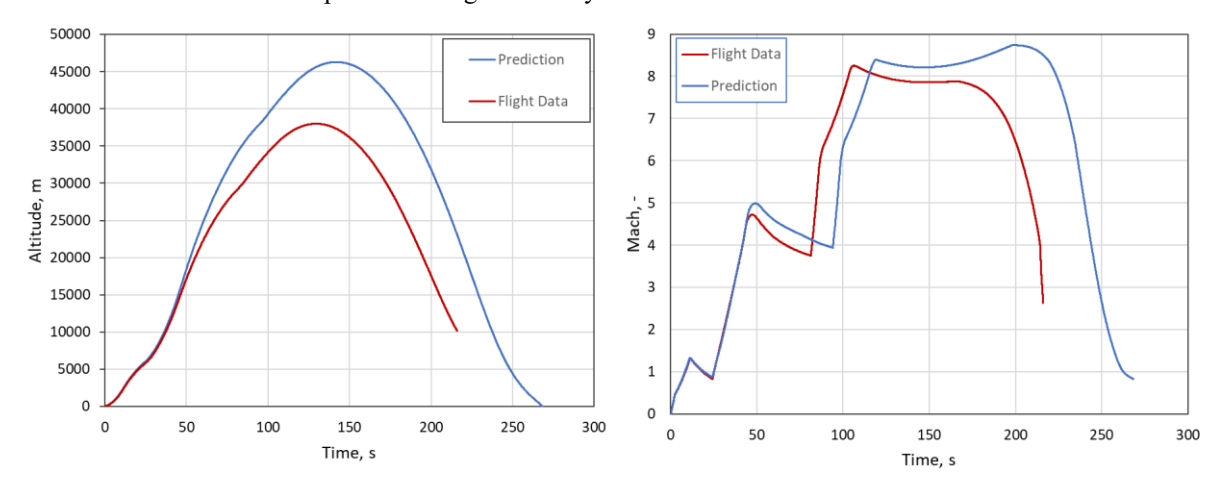


Figure 9: STORT trajectory data.

b) Mach number as achieved and predicted

a) Altitude as achieved and predicted

Table 2: Characteristic flight events and their corresponding times.

Event	Time, s	
Lift-off, ignition 1st stage	0	
Burnout 1st stage	11.4	
Ignition 2 nd stage	24.25	
Burnout 2 nd stage	48.2	
Ignition 3 rd stage	81.3	
Burnout 3 rd stage	107.1	
Apogee	169	
Impact	>277	

5.1 Tip

In Figure 10 the temperatures measured in the tip of the forebody are presented. When the graphs are compared to the flight trajectory in Figure 9 it is obvious that the temperatures develop according to the velocity of the vehicle, with a certain delay due to the fact of the thermal capacitance of the structure. The first two increases in temperature up to roughly 50 seconds are corresponding to the velocity increase during the first and second stage burn, with the increase

due to the second stage burn much higher as the velocity increase is much bigger. Then, during the coast phase between second and third stage, the temperature levels out until, at approximately 90 seconds, it starts to rise again after the third stage ignition. It keeps rising even after the third stage has burned out since the velocity stays at a high Mach number until roughly 200 seconds. The event of the burnout of the third stage is visible in the data, the gradient of the temperature increase goes down slightly after approximately 110 seconds.

Towards the end of the data set, the foremost thermocouple drops off quite rapidly after 210 seconds, whereas the other two thermocouples show an even steeper increase in temperature for a short time at 200 seconds. The exact cause of that behavior is unknown, but assumptions can be made, especially when the temperature data of the downstream segments are compared. The maximum temperature in the nose that was measured was 1111°C at TS002V. At TS003V the maximum temperature was 635°C and at TS004V the maximum was 701°C. Up to these events, the gradient of the temperature increases during and after the third stage burn is almost constant and indicates that the structure has not yet reached a steady-state condition with regard to the temperature.

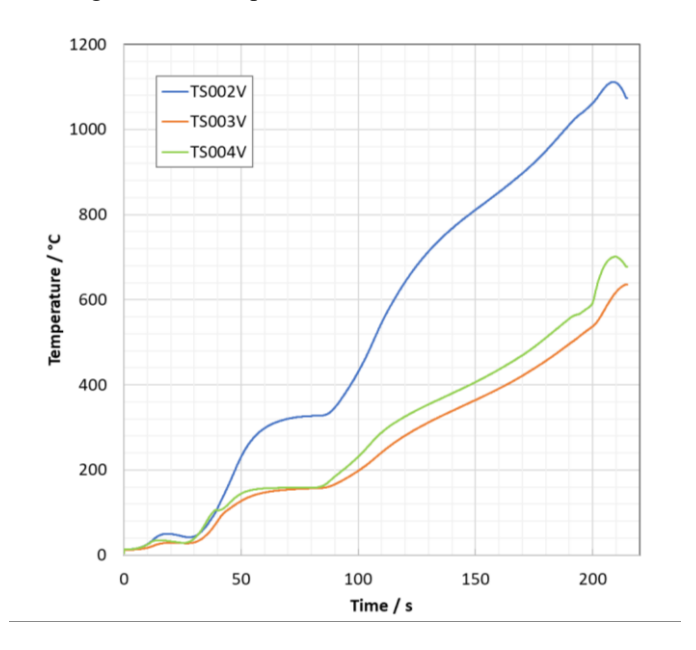


Figure 10: Measured temperatures in the CMC nose tip.

5.2 Segment A

The measured temperatures in segment A are shown in Figure 11. Also for this segment of the forebody, there is a small increase of all temperatures as a result of the first stage burn and a much higher increase due to the second stage burn. It is interesting to note, that the temperatures of the aft end of this segment increase to significantly higher levels than those measured at the front end. The difference is on the order of 150 K. The temperature difference remains in principle also during the coast phase between the second and third stage burn and after the third stage burnout when the vehicle goes through apogee and finally dives to a low altitude. The reason for this behavior is the fact that the nose is a structure made from a solid block of material, whereas on segment A, the CMC structure is a relatively thin-walled shell. At the front end of segment A, the CMC shell structure is in contact to the solid nose and heat is transferred into the heat sink of the solid nose, reducing the temperature at the front end of the segment A CMC shell.

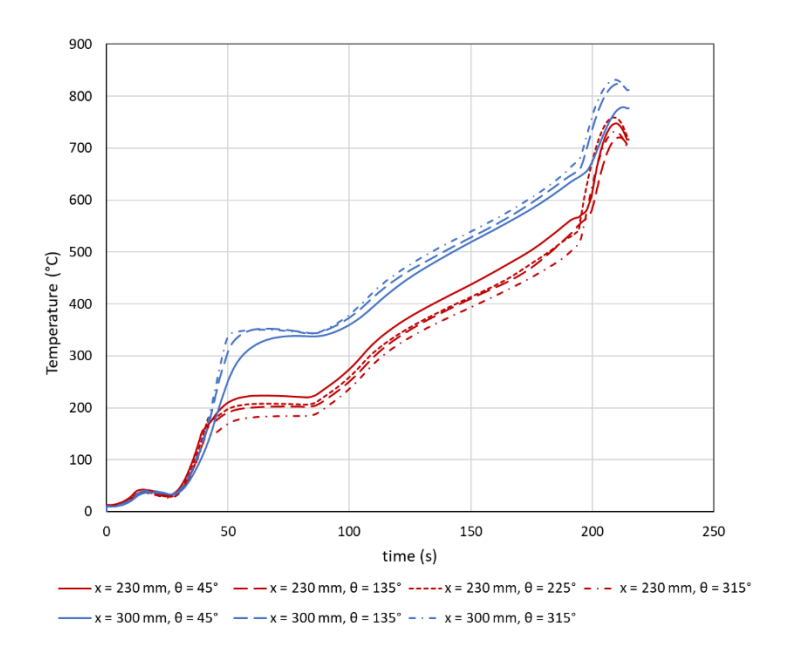


Figure 11: Measured temperatures in segment A.

Also in the temperature data on segment A, the slight decrease of the gradient of the temperature increase after the burnout of the third stage is visible. Following this, the temperatures increase in an almost linear way until a sudden and significant increase is visible for all thermocouples in segment A just before 200 seconds. The appearance of this rise is slightly earlier than in the tip.

5.3 Segment B

The measured temperatures for segment B are shown in Figure 12. In general, the temperatures also increase as the velocity of the vehicle increases. The development of the temperatures is quite similar to that on segment A with a small increase during the first stage burn and a larger increase during the second stage burn. On segment B the temperatures measured at the front end at the position of x = 410 mm are higher than that measured at the end, which is what is expected, in contrast to what was seen on segment A. Similar to the data from the tip and segment A, also in the case of segment B the change of the gradient of the temperature increase after the burnout of the third stage is visible at roughly 110 seconds.

A noticeable difference is, that the temperature increase towards the end of the flight is even earlier than for segment A and it seems to be not as sharp but more gradually setting on. Another feature of interest is, that the data of the 45° sensor at the position of x = 410 mm stands out. It rises to higher values during the second stage burn than the other sensors at the same x position. The cause is not known exactly. During and after the third stage burn, the 45° sensor is again quite close to the other sensors.

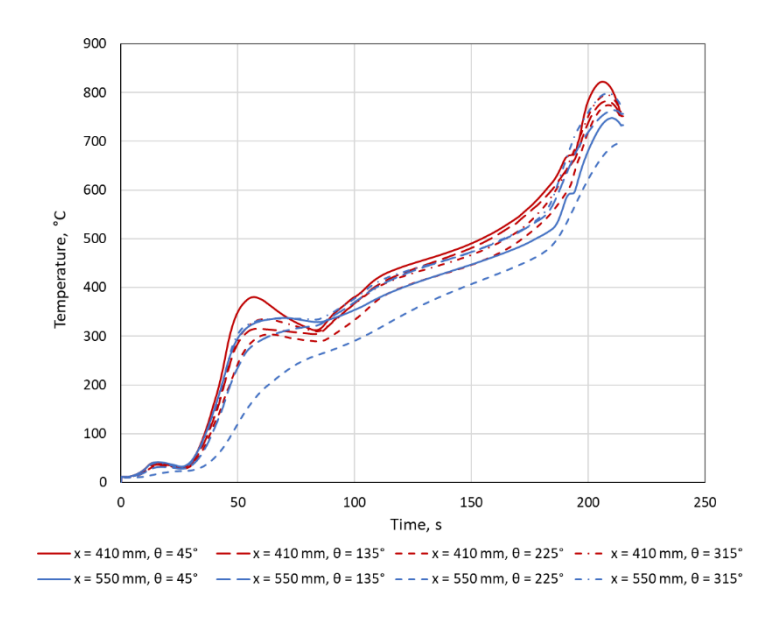


Figure 12: Measured and simulated temperatures in segment B.

5.4 Segment C

In Figure 13 the measured temperatures on the CMC structure of segment C are presented. Here, the measurements are all really close together. The temperature increases over time in general follows a similar pattern as described before, with the three distinct increases as a result of the velocity increase of the rocket. The temperature increase towards the end of the flight appears earlier for segment C than for segments A and B upstream. Due to the fact, that it starts earlier, also the relative height of this increase is larger.

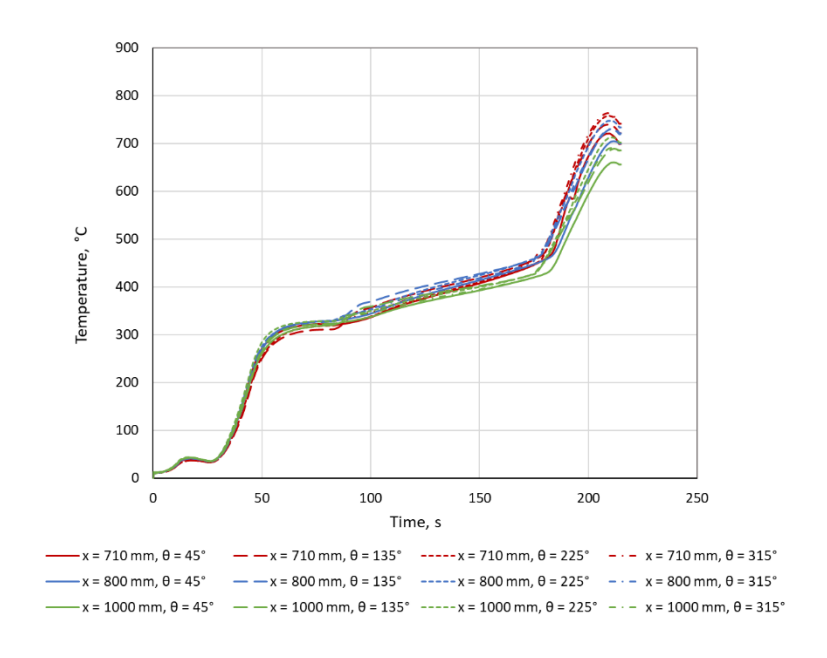


Figure 13: Measured temperatures in segment C.

5.5 Segment D

In Figure 14 the measured temperatures on the CMC structure of segment D are shown. It was the segment that is at the very end of the CMC forebody. It seems that the temperature after the second stage burn is in fact slightly decreasing

for some measurement positions at the end of the coast phase before the third stage ignition. In addition, it is noteworthy that the increase of the temperatures during the high Mach number flight phase is almost linear. The increase of the temperatures towards the end of the flight appears even earlier than for segment C and the other upstream segments. Also the relative height of the increase is the largest. It seems to be a fair speculation that this increase is due to the transition of the flow from laminar to turbulent behavior, and thus to an increase in heat flux.

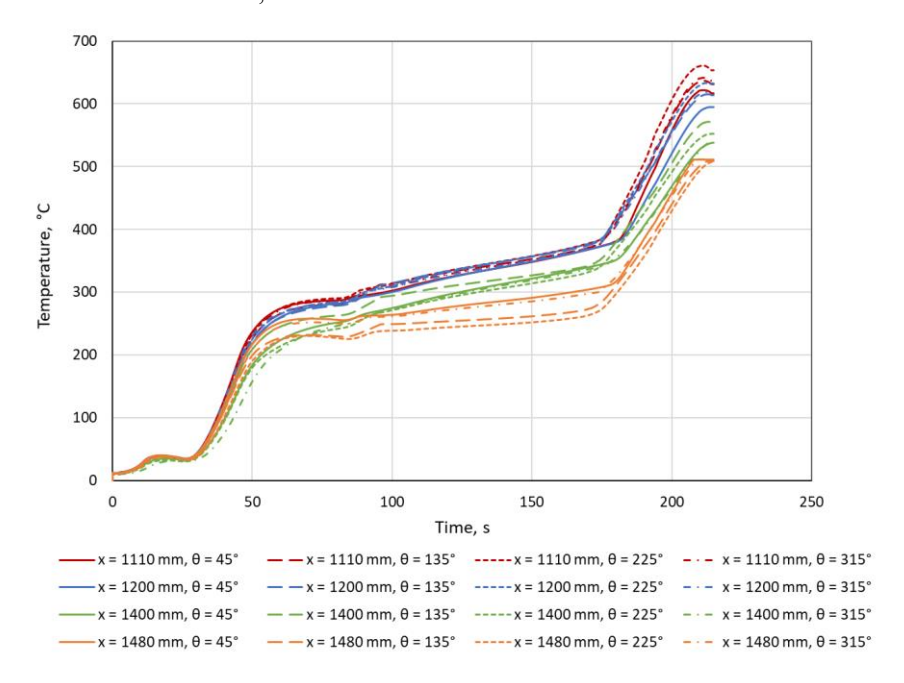


Figure 14: Measured temperatures in segment D.

5.6 Connection elements

One question of interest was, how the temperatures at the connection between CMC and metallic structures developed. The CMC shells were connected to the metallic structure via the so-called double-I connections. At two positions, on one connection on segment B and one connection on segment C, the temperature was measured on the CMC bracket and also on the corresponding metallic bracket. The measured data is shown in Figure 15.

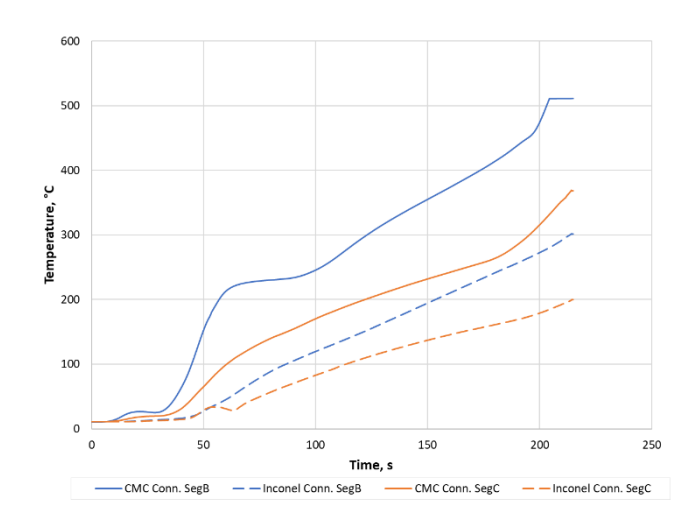


Figure 15: Measured temperatures in two of the double-I connections, one of segment B and C.

It can be noted that the temperature of the metallic bracket stayed below 300 °C which is well below the acceptable temperature of the used Inconel material.

5.7 Internal structure

One more aspect that should be investigated was the issue of the temperature rise of the metallic structure as such. Since the vehicle was quite small and there was no cooling system installed (except for the canards as an experiment), the forebody metallic structure acted also as a heat sink to keep the temperatures at an acceptable level for the electronics installed inside. In Figure 16 the measured temperatures in the different structure segments are shown. The measurement position was at the back end of each of the segments. It can be noted that the temperatures remained quite low in general with the exception of the interface ring between forebody and the canard module which was going up quite fast at the end of the flight but still remained at acceptable values. Interesting is that the temperature measured in segment D was rising sooner and faster than those measured in segment A, B and C.

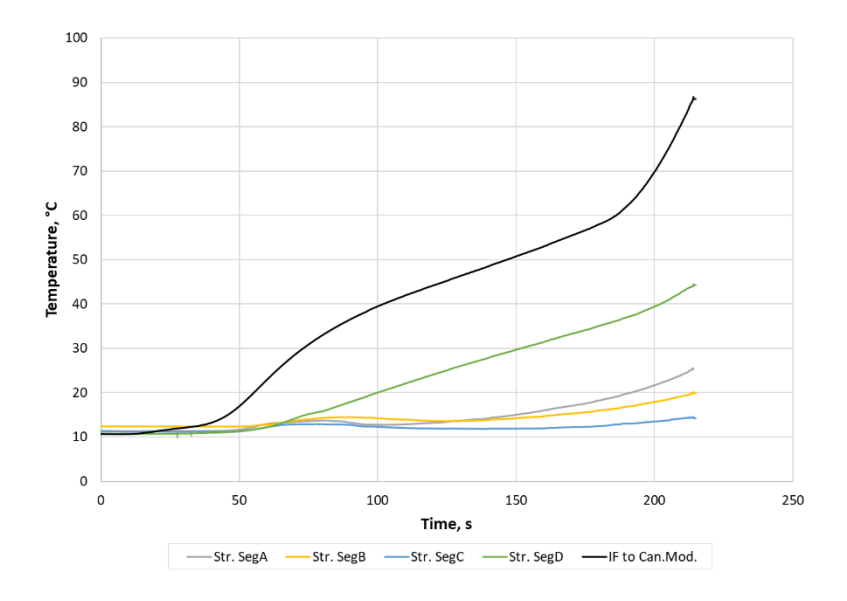


Figure 16: Measured temperatures in the metallic internal structure.

5.8 Transition Time

From the temperature data, the time of the transition of the flow from laminar to turbulent was determined as good as possible. For each measurement position the temperature gradient was calculated and plotted, then the time of the significant change in the gradient of the temperature increase was determined. In Figure 17 the temperature gradients at the x-position of 1000 mm in segment C are plotted over time. In comparison to the temperature plot in Figure 13 it is clearer to determine the onset of the temperature increase.

In Figure 18 the temperature gradients at x=1000 mm are plotted over time, but for a shorter time window of 30 seconds. The transition time can be fairly well established. There are also interesting other features, as e.g. certain temperature oscillations.

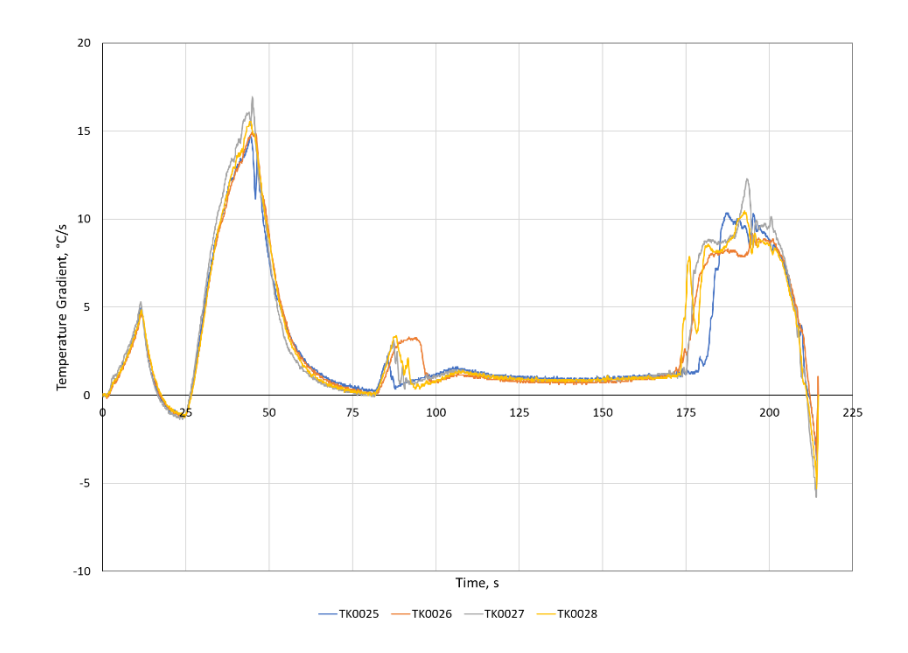


Figure 17: Temperature gradients at the axial position of x = 1000 mm.

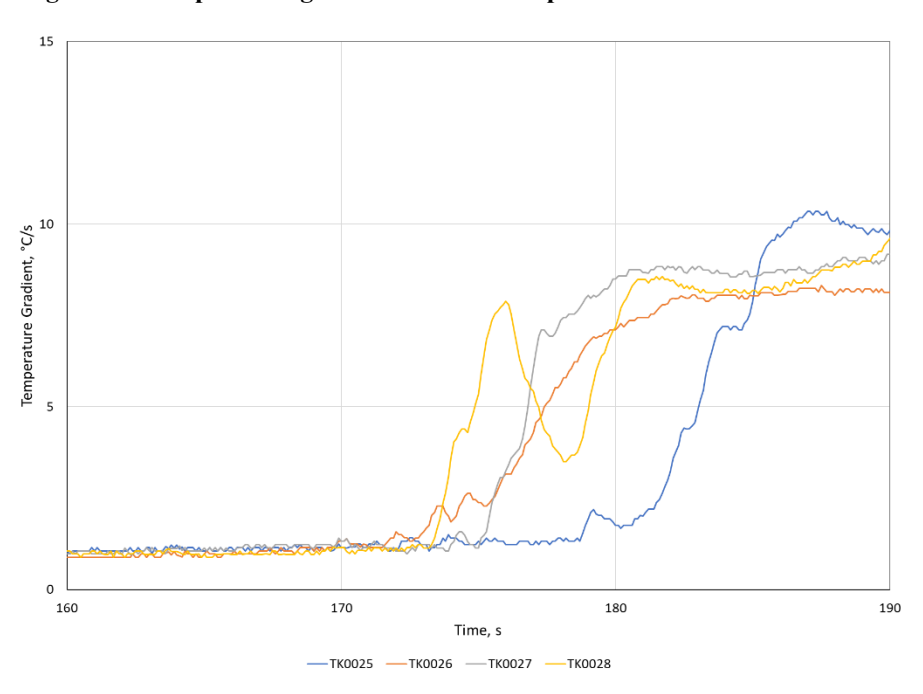


Figure 18: Temperature gradients at x=1000 mm around the time of transition.

The determined transitions times for the TPS temperature sensors can be plotted against the x-position of the sensor, which is the distance from the stagnation point. In doing so, there is a clear correlation between the x-position and the transition time. The data can be separated even more to reflect the four measurement planes at the angles 45°, 135° 225° and 315° which gives additional information. However, with regard to this, it will be presented in a following publication.

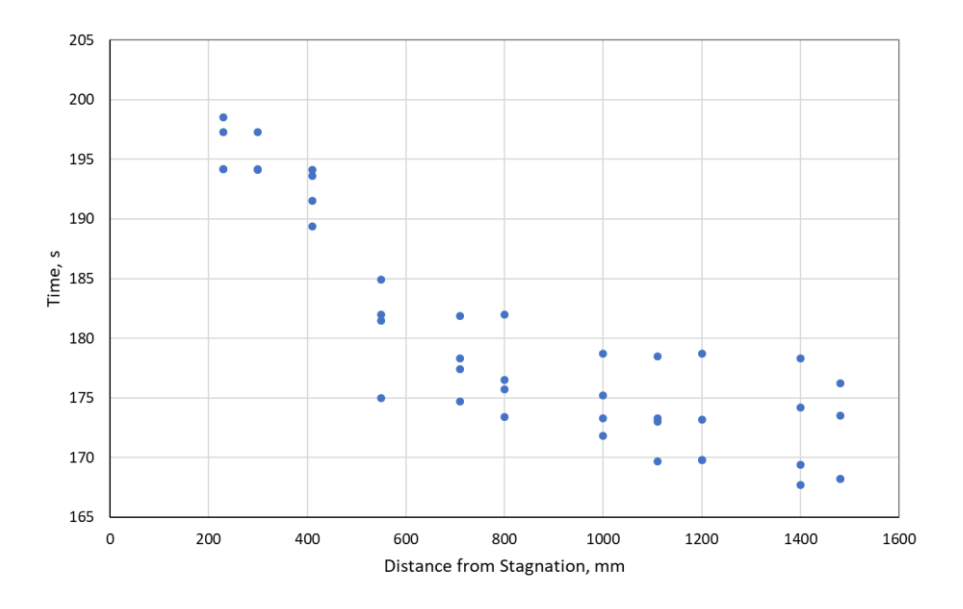


Figure 19: Transition times at different axial positions on the TPS.

5.9 Heat flux load as calculated from temperature data

From the measured temperature data of the thermocouples, the surface heat flux as the driving load for the thermocouple temperature can also be calculated iteratively. Since the thermocouples were located close to the surface, it is assumed that a one-dimensional analysis is appropriate to simulate the conditions. For each thermocouple position, the actual distance from the surface and the actual wall thickness of the CMC structure was determined before the flight via a computer tomography scan. Using this data and the insulation thickness of 20 mm as well as the structure thickness of the metallic substructure, a 1-D model was built with a surface heat flux as the load and a boundary condition of radiation to the environment at the surface. At the lower boundary of the metallic substructure, an adiabatic boundary was set. With this model, a surface heat flux was applied and the resulting temperature at the thermocouple position at the specified depth was used as the control value to increase or decrease the heat flux value until the resulting temperature matched the measured flight data to a sufficient accuracy. After some iterations, the surface heat flux density profile is achieved and it is shown for the measurement position of TK0026 at segment C in Figure 20. TK0026 was located at x=1000 mm at the angular plane of 315°.

The simulated heat flux profile is corresponding well to the flight events, as there are the velocity increases due to the booster stages operation, and it also reflects the big increase in heat flux at the end of the flight as a result of the suspected transition from laminar to turbulent flow. At this point the heat flux values shall not be further discussed in detail, only so far as it is noteworthy to see that as the result of this simulation the heat flux before transition was on the order of 30 kW/m², whereas after transitioning it increased to roughly 140 kW/m². The double-peak towards the end of the flight needs to be confirmed by more data analysis of other positions.

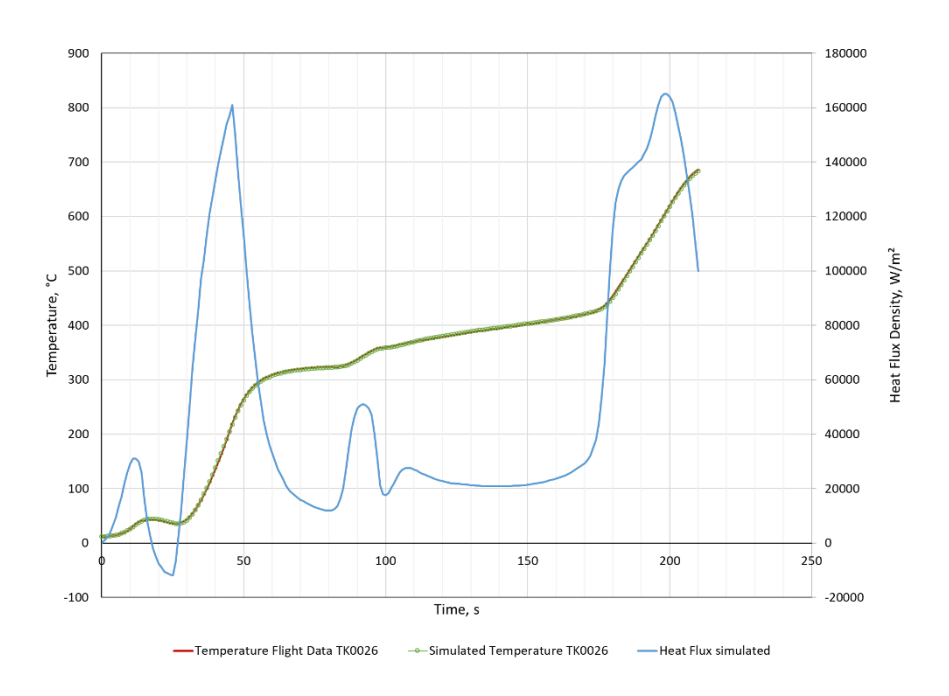


Figure 20: Temperature flight data of TK0026 and corresponding heat flux density.

6. Conclusion

Understanding the hypersonic flight regime is a key element in the development of space transportation vehicles that needs to be investigated, in particular also for reusable vehicles. In the STORT project a flight experiment with a three-stage sounding rocket and the so-called forebody as the payload was carried out that aimed at collecting flight data during a hypersonic flight of the vehicle. The forebody of the vehicle, on top of the third stage was designed as a pointed slender body with axial symmetry. Because of the expected high temperatures, the surface of the forebody was covered with a TPS that was made fully from CMC material. The material from which the surface structures of the TPS were made is C/C-SiC which is produced in-house at DLR. In order to have a detailed picture about the thermal environment during the flight, a large number of sensors were integrated in the TPS. Among the sensors were mainly thermocouples but also pressure sensors and coaxial thermocouples to measure heat flux. In this work the data collected by the thermocouples on various structures of the TPS was presented and some calculations and conclusions were drawn from it.

As it was shown before, the measured temperatures on the structures increase, the closer the distance to the stagnation point is. The maximum measured temperatures on the tip are 1111°C, which was measured at a distance from 34 mm from stagnation and off-center at a depth of 5 mm from the surface. This is much lower than the expected stagnation temperature, however, it has to be considered that the solid nose tip was a huge heat sink mass. In general it can be said, that the thermal environment during the phase of the flight where the Mach number was at a high level was still not at a steady-state but the temperatures were increasing all the time.

Especially towards the end of the flight, an interesting phenomenon of a temperature rise occurred at all measurement positions, which is attributed to the transition from laminar to turbulent flow. The magnitude of this temperature increase is significant and was on the order of 200 to 300 degrees Celsius.

In order to have a better understanding of what happened, the point in time was determined at which the temperatures started to increase. In doing so, it could be shown that the temperatures start to rise first at the back end of the vehicle and then the increase occurs at later times at more forward positions. This seems to make sense in terms of laminar to turbulent transition.

In addition, an effort was made to calculate the transient heat flux profile from the temperature data of one of the sensors, which was the TK0026 thermocouple at the x-position of 1000 mm on segment C, to get quantitative information about the magnitude of the heat flux increase that drives the temperature increase. The heat flux profile could be determined and it is very interesting to see, that the value of the heat flux which is calculated is on the order of $140 \, \text{kW/m}^2$ for the turbulent case, in comparison to roughly $30 \, \text{kW/m}^2$ for the laminar case. This is a very important result as it shows that the transition from laminar to turbulent flow goes along with a massive increase in heat flux density. In general, this conclusion is not new, but it is relevant in so far, as it gives realistic numbers derived from flight data collected in a representative flight environment. In addition, it has to be kept in mind that the temperatures were still increasing overall due to the relatively short mission flight time, which means that if longer flights are considered, the issue of flow transition with higher heat fluxes due to turbulent flow becomes very important.

With regard to the measurements carried out by thermocouples and their usefulness to determine the thermal environment it can be said that this method has proven to be very effective while relying on simple sensors. In a future effort, this procedure of the temperature data processing and the calculation of the heat flux will be applied to the other temperature sensors on the forebody as well.

References

- [1] H. Weihs, J. Longo, J. Turner, The Sharp Edge Flight Experiment SHEFEX II, a Mission Overview and Status, 15th AIAA International Space Planes and Hypersonic Systems and Technologies Conference, AIAA 2008-2542, 2008.
- [2] W. Bauer, et al., DLR Reusability Flight Experiment ReFEx. Acta Astronautica, 168 (2019), pp. 57-68. DOI: 10.1016/j.actaastro.2019.11.034
- [3] S. Guédron, S. Ishimoto, E. Dumont, CALLISTO: a Cooperation for an In-Flight Demonstration of Reusability, 70th International Astronautical Congress (IAC), 21-25 October 2019, Washington DC, USA.
- [4] A. Gülhan, D. Hargarten, M. Zurkaulen, F. Klingenberg, F. Siebe, S. Willems, G. Di Martino, T. Reimer, Selected Results of the Hypersonic Flight Experiment STORT. Acta Astronautica 211 (2023), pp. 333-343. https://doi.org/10.1016/j.actaastro.2023.06.034
- [5] R. Kochendorfer, N. Lutzenburger, H. Weihs, Joining Techniques for Fibre Ceramic Structures, *Advanced Composites Letters*, 13 (1) (2004). DOI: 10.1177/096369350401300106
 - [6] Van Driest, E.R., The Problem of Aerodynamic Heating, Aeronaut. Eng. Review, Vol. 15 No. 10, 1956.
- [7] Di Martino, G.D., Reimer, T., Dauth, L., Baier, L., Structure Design of a Sounding Rocket Fairing with a Segmented Filament Winding-Ceramic Matrix Composite Thermal Protection System, HiSST: 2nd International Conference on High-Speed Vehicle Science Technology, 11–15 September 2022, Bruges, Belgium.